Analysis of extinction characteristics of non-spherical biological particle aggregates [Invited]

Guolong Chen (陈国龙)[1,2], Youlin Gu (顾有林)[1,2,3,*], Yihua Hu (胡以华)[1,2,3], Fanhao Meng (孟凡昊)[1,2,3], Wanying Ding (丁婉莹)[1,2], and Xi Zhang (张 熙)[1,2]

[1] National University of Defense Technology, Hefei 230037, China
[2] State Key Laboratory of Pulsed Power Laser Technology, National University of Defense Technology, Hefei 230037, China
[3] Advanced Laser Technology Laboratory of Anhui Province, Hefei 230037, China

In this study, a method was presented to accurately obtain the extinction characteristics of the non-spherical biological particle aggregates. Based on the multi-sphere particle model of non-spherical particles, a randomly oriented aggregation model was firstly built to construct the aggregates. The discrete-dipole approximation method was used to calculate the extinction characteristics of aggregates in the 3–14 μm waveband. The average mass extinction coefficients of three materials are 0.802 m²/g, 0.907 m²/g, and 0.866 m²/g in the 3–5 μm waveband and 0.590 m²/g, 0.402 m²/g, and 0.523 m²/g in the 8–14 μm band, respectively. Smoke chamber experimental results are in good agreement with theoretical analyses.

Keywords: non-spherical aggregates; biological particle; random orientation; extinction characteristics.
DOI: 10.3788/COL202321.090003

1. Introduction

As a novel extinction material, biological materials have attracted wide attention due to their advantages such as low preparation cost, environmental protection, non-toxic, easy degradation, and wide extinction band[1-3]. Gu *et al.*[4] studied the effect of the activity of biological materials on their average mass extinction coefficient (MEC) and presented a practical method to discriminate the viable and dead microbes. Wang *et al.*[5] found that when the relative humidity of air exceeds 70%, the ratio of attenuation rate to concentration increases with relative humidity. Generally, biological materials are composed of artificially prepared biological particles, and biological particles have abundant sources and different morphologies[6], such as spherical, ellipsoidal, cylindrical, and irregular shapes. When released into the air, biological particles exist in the form of aggregates with complex spatial structures[7] and can attenuate light. With the widespread application of photoelectric detection systems, biomaterials with strong extinction performance have aroused great interest in research and practical applications.

The extinction characteristics of biomaterials have been widely studied by theoretical calculation. The extinction efficiency factor of different-shaped biological particles was calculated[8,9], and the extinction characteristics of the monodisperse[4,7,10,11] and polydisperse[12] biological particle aggregates have been explored. However, previous models for calculating the extinction characteristics of biomaterials used spherical particles for aggregation, without considering the aggregation of irregularly shaped particles, and without considering the numerical simulation of randomly oriented irregular particle aggregation. Currently, no published literatures on the extinction characteristics of non-spherical biological particle aggregates with random orientations were found. Therefore, establishing a method to accurately obtain the extinction characteristics of the non-spherical biological particle aggregates is an important challenge.

Research on the extinction characteristics of aggregates mainly relies on the build of the aggregation model. At present, there are many aggregation models[13,14] available for the aggregation of spherical particles, some of which can be used for the fixedly oriented[15] and randomly oriented[16] aggregation of elliptical particles. However, there are no reports on the universal aggregation models for non-spherical particles, especially the randomly oriented aggregation model for irregularly shaped particles. The essential difficulty for the aggregation simulation of non-spherical particles lies in devising an accurate and efficient algorithm for detecting the contact between particles. Therefore, various particle models have been proposed for accurately describing the shape of the non-spherical particle, such as the multi-sphere model, super-ellipsoid model, and polyhedral model[17]. With the high contact detection efficiency and robustness, the multi-sphere model appears to be the most commonly used particle model in researches on particle conveying, material

mixture, and particle deposition[18]. The multi-sphere model has potential application value in the construction of non-spherical particle aggregation (NSPA) models.

In this work, the extinction characteristics of the non-spherical biological particle aggregates were studied through theoretical calculation and experimental verification. The aggregates of three non-spherical biological particle materials were constructed by using the NSPA simulation code. Based on materials' reflectance spectra measured by a Fourier transform infrared spectrometer, the discrete-dipole approximation method (DDA)[19] was used to calculate the MECs of aggregates. A large smoke box experimental system was designed to validate the feasibility and effectiveness of the proposed method.

2. Materials and Methods

To investigate the extinction characteristics of non-spherical biological particle aggregates, three types of microbial materials, which are AN2301, BB2302, and AO2303, were prepared through the process of strain activation, shaking flask culture, large tank fermentation, centrifugation, pure water cleaning, vacuum freezing and drying, and grinding by a superfine Chinese medicine grinder[20].

As shown in Fig. 1, AN2301 is pumpkin shaped, the ratio of its height to diameter is about 1 : 2, and the diameter is between 3.6 and 4.2 μm. BB2302 is with a single-sided concave pancake shape, where the ratio of the thickness to the diameter is about 1 : 3, the diameter is between 1.8 and 2.2 μm, and the depth of the concave surface is 0.3 μm. AO2303 is cylindrical (aspect ratio is 1.2 : 1), ellipsoid (aspect ratio is 1.2 : 1), and spherical, accounting for 50%, 20%, and 30% respectively, and the particle size is evenly distributed between 2.2 and 3.4 μm. The aggregates containing 10, 20, and 30 particles, respectively, were assumed to analyze the extinction characteristics.

2.1. Randomly oriented aggregation model of non-spherical particles

The multi-sphere model[17] was used to build the shape of the non-spherical particles, rather than simply equating them to spherical particles of equal volume. The aggregated spatial structure was constructed by using the NSPA simulation code, which realized the Monte Carlo simulation of the randomly oriented motion of non-spherical particles. In the simulation program, the randomly oriented motion of non-spherical particles in three-dimensional space is simulated through the rotation
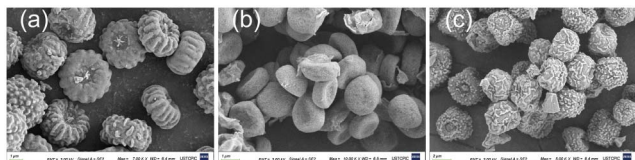

Fig. 1. Scanning electron micrographs of microbial materials. (a) AN2301. (b) BB2302. (c) AO2303.

of random angles and the movement of random directions during the aggregation process of non-spherical particles, rather than the motion in a specific direction. Three hundred aggregates were generated for each of the three materials. Figure 2 partly shows the obtained aggregates with different particles number N.

Porosity is an important parameter to describe the spatial structure characteristics of aggregates and can be calculated according to the aggregated geometry[21]. The following parameters were used to describe the geometry of aggregates. The volume of the ith particle is denoted by V_i, the porosity of the aggregation is denoted by P, and the radius of gyration is denoted by R_g. The relationship between N and R_g is approximated as[21]

$$R_g^2 = \frac{1}{2N^2} \sum_{i=1}^{N} \sum_{j=1}^{N} |r_i - r_j|^2, \qquad (1)$$

where r_i and r_j are the coordinates in space of the ith and jth particles, respectively. The effective radius R_e of the aggregates can be obtained as

$$R_e = \sqrt[3]{\sum_{i=1}^{N} \frac{3V_i}{4\pi}}. \qquad (2)$$

The porosity of the aggregated particles is given by[22,23]

$$P = 1 - \left(\frac{\sqrt{3/5} R_e}{R_g} \right)^3. \qquad (3)$$

The larger the porosity is, the looser the spatial structure of the aggregates is. Three materials have different particle shapes and particle size distributions, so their aggregates have different porosity distributions. As shown in Fig. 3, the average porosity increases as the number of particles contained in the aggregate increases. Among the three materials, the particles of BB2302 are
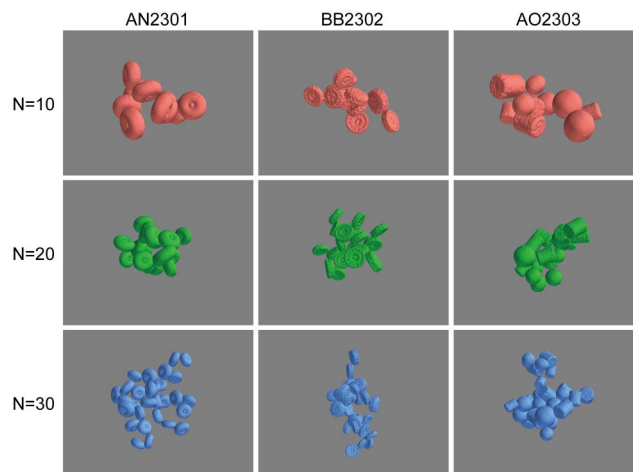

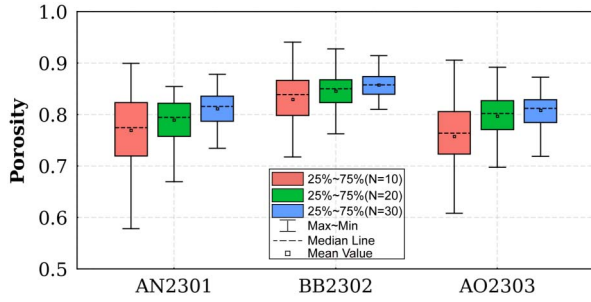**Fig. 2.** Spatial structures of aggregates.

Fig. 3. Porosity distributions of aggregates.

Fig. 5. Complex refractive indices of three materials in the 2.5–25 µm waveband. (a) Real parts of the complex refractive indices. (b) Imaginary parts of the complex refractive indices.

the least spherical, so the average porosity is also larger than the others.

Non-spherical particle aggregates with different shapes have different spatial structures, radii of gyration, and porosity, resulting in different equivalent complex refractive indices[24] and extinction characteristics[12]. Adopting a spherical approximation aggregation model will result in the spatial structure differences of particle aggregates with different particle shapes being ignored, leading to an increase in the calculation error of extinction characteristics.

2.2. Complex refractive index calculation model

To obtain spectral reflectance, the tablets of three samples were prepared with the pressure of 30 MPa using the tablet machine. The tablets, with a fixed mass at 1.8 g, had a diameter of 3 cm and thickness of 0.8–1.2 mm, and the surfaces were as smooth as possible. As shown in Fig. 4, the specular reflectance in the 2.5 to 25 µm waveband was measured by the Nicolet 8700 Fourier transform infrared spectrometer (Thermo Fisher Scientific, USA).

According to the Kramers–Kronig (K-K) relation[25,26], the reflective phase shift Θ_λ can be expressed as[27]

$$\Theta_\lambda = \frac{\lambda}{\pi} P \int_0^\infty \frac{\ln R_{\lambda'}}{\lambda'^2 - \lambda^2} \mathrm{d}\lambda', \qquad (4)$$

where λ is the wavelength, P is the Cauchy principal value function, and $R_{\lambda'}$ is the vertical reflectivity.

The real parts (n_λ) and imaginary parts (k_λ) of the complex refractive index values m_λ ($m_\lambda = n_\lambda + ik_\lambda$) can be obtained by[27]
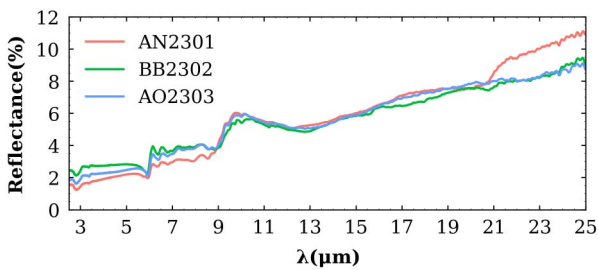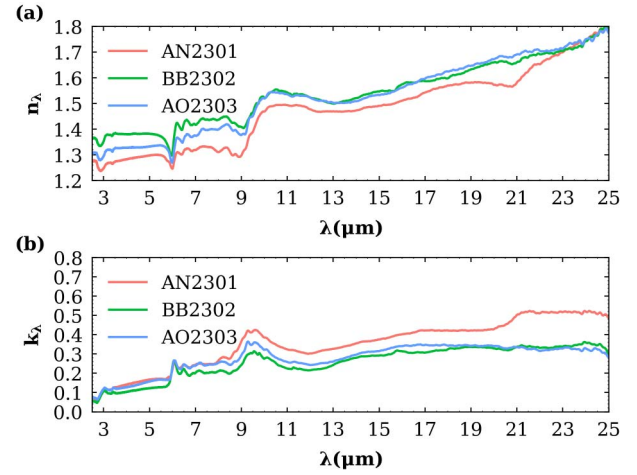

Fig. 4. Specular reflectance of three materials in the 2.5–25 µm waveband.

$$n_\lambda = \frac{1 - R_\lambda}{1 + R_\lambda + 2\sqrt{R_\lambda}\,\cos\Theta_\lambda}, \qquad (5)$$

$$k_\lambda = \frac{-2\sqrt{R_\lambda}\,\sin\Theta_\lambda}{1 + R_\lambda + 2\sqrt{R_\lambda}\,\cos\Theta_\lambda}. \qquad (6)$$

It is known that the R_λ should be obtained in the full band to calculate the complex refractive index. However, in actual experimental measurements, the R_λ can be measured only in the limited band (2.5–25 µm). To supplement the missing reflectivity spectrum when calculating the integral, the reflectivities at wavelengths below 2.5 µm are assumed to equal the reflectivity at 2.5 µm, and the reflectivities above 25 µm are equal to the reflectivity at 25 µm, represented as $R_{(0-2.5\,\mu m)} = R_{2.5\,\mu m}$ and $R_{(25-100\,\mu m)} = R_{25\,\mu m}$. Therefore, R_λ over the entire integral range (0–100 µm) was acquired. A value of 100 µm was used as the upper limit of the integral because the reflectivity above 100 µm had little influence on the complex refractive index in the 2.5–25 µm wavelength range[28,29]. The complex refractive indices of the three materials were obtained, as shown in Fig. 5.

2.3. Extinction calculation model for aggregates

Based on the obtained aggregates and the complex refractive index of materials, the DDA method was used to calculate the absorption efficiency factor Q_{abs} and the scattering efficiency factor Q_{sca}. The numerically exact DDA method is completely flexible regarding the geometry of the target and is limited only by the need to use an inter dipole separation d that satisfies $|m_\lambda|kd < 0.5$ ($k = 2\pi/\lambda$) for an accurate solution[30,31]. In this study, the DDA code discrete-dipole scattering (DDSCAT) was used to calculate the scattering and absorption of aggregates. The 'GKDLDR' option in the DDSCAT was selected, which specifies that the surface-corrected lattice dispersion relation[30,32] approach of the polarizability prescription was used to determine the dipole polarizabilities for the extinction

calculation of aggregates. Good accuracy can be achieved because the complex refractive index values m_λ of the three materials satisfied $|m_\lambda - 1| < 0.8$[30]. The Q_{abs} and Q_{sca} can be calculated in the execution of the DDSCAT by[19]

$$Q_{abs} = \frac{4k}{R_e^2 |\overrightarrow{E}_{inc}|^2} \sum_{j=1}^{N_d} \left\{ \mathrm{Im}[\overrightarrow{P}_j \cdot (\alpha_j^{-1})^* \cdot \overrightarrow{P}_j^*] - \frac{2}{3} k^3 |\overrightarrow{P}_j|^2 \right\}, \tag{7}$$

$$Q_{sca} = \frac{k^4}{\pi R_e^2 |\overrightarrow{E}_{inc}|^2} \int d\Omega \left| \sum_{j=1}^{N_d} [\overrightarrow{P}_j - \hat{n}(\hat{n} \cdot \overrightarrow{P}_j)] e^{-ik\hat{n} \cdot \overrightarrow{r}_j} \right|^2, \tag{8}$$

where k is the wave vector of incident light, R_e is the effective radius of non-spherical biological particle aggregation, $\overrightarrow{E}_{inc}$ is the electric field strength vectors of incident light, and N_d is the number of dipoles. $\overrightarrow{P}_j$ is the dipole moment of the jth dipole, α_j is the polarizability of the jth dipole, $d\Omega$ indicates the microelements of the solid angle, $\hat{n}$ is the unit vector of the scattering direction, $\overrightarrow{r}_j$ is the coordinate vector of the jth dipole, superscript * represents the complex conjugate, and Im is the complex imaginary part.

The extinction efficiency factor Q_{ext} can be calculated by

$$Q_{ext} = Q_{abs} + Q_{sca}. \tag{9}$$

The MEC value of the aggregate can be defined as the ratio of the extinction cross section of the aggregate to its mass. The mass densities ρ of the three non-spherical biological particle materials are $0.732 \, \mathrm{g/cm^3}$, $0.805 \, \mathrm{g/cm^3}$, and $0.806 \, \mathrm{g/cm^3}$, respectively. The MEC of aggregates at each wavelength can be given as

$$\mathrm{MEC} = \frac{3Q_{ext}}{4\rho R_e^2}. \tag{10}$$

Then, the average MEC of aggregates in the $\lambda_1 - \lambda_2$ waveband can be obtained by

$$\mathrm{MEC}_{(\lambda_1 - \lambda_2)} = \int_{\lambda_1}^{\lambda_2} \mathrm{MEC}_\lambda / (\lambda_2 - \lambda_1) d\lambda. \tag{11}$$

3. Results and Discussions

3.1. Extinction calculation results

The MEC is an important parameter to characterize the extinction performance of the aggregate. The average MECs of the aggregates in the 3–5 μm (mid infrared, MIR) and 8–14 μm (far infrared, FIR) wavebands are shown in Table 1.

As the number of particles contained in the aggregates changes from 10 to 30, the average MECs of BB2302 increase, while the situation of AN2301 is the opposite. For AO2303, the extinction ability is weakened in the MIR, while it is enhanced in the FIR.

Table 1. Average MECs of Aggregates with Different Particle Numbers in the 3–5 μm and 8–14 μm wavebands.

Material	N	R_e (μm)	3–5 μm		8–14 μm	
			Q_{ext}	MEC (m²/g)	Q_{ext}	MEC (m²/g)
AN2301	10	3.825	3.143	0.842	2.255	0.604
	20	4.818	3.743	0.796	2.773	0.590
	30	5.514	4.130	0.767	3.099	0.576
BB2302	10	1.720	1.629	0.883	0.720	0.390
	20	2.166	2.123	0.913	0.941	0.405
	30	2.479	2.458	0.924	1.093	0.411
AO2303	10	3.104	3.000	0.900	1.731	0.519
	20	3.878	3.597	0.863	2.184	0.524
	30	4.430	3.971	0.834	2.505	0.526

The extinction ability of aggregates mainly stems from the absorption and scattering effects of light. The theoretical calculation MEC values at each wavelength λ in the range of 3–14 μm are shown in Fig. 6. The proportion of absorption and scattering to extinction is different at different wavelengths. The infrared absorption ability is closely related to the functional groups of the material, and the three materials exhibit similar strong absorption abilities at 6.1 μm and 9.5 μm.

Moreover, the size of the aggregate has an important impact on its scattering ability. In the 3–5 μm waveband, because the effective radius R_e of the aggregates is close to the wavelengths, the scattering effect is strong, which may be explained by the Lorenz–Mie theory. In the 8–14 μm waveband, due to significant weakening of the scattering ability, the extinction ability is dominated by absorption. The three materials have similar functional
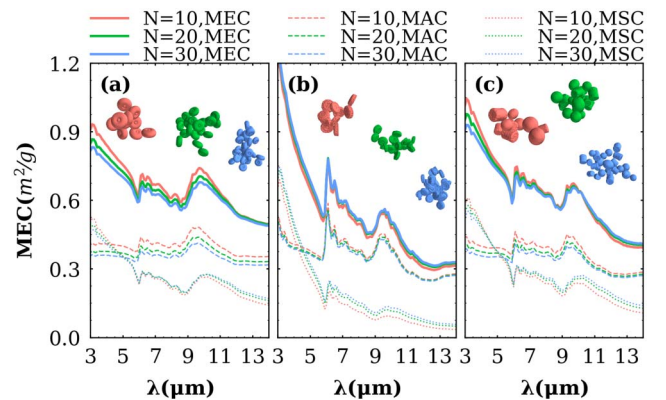

Fig. 6. MECs of three materials in the 3–14 μm waveband. The dashed line represents the MEC corresponding to the absorption effect, marked as MAC, while the dotted line represents the MEC corresponding to the scattering effect, marked as MSC. (a) AN2301. (b) BB2302. (c) AO2303.
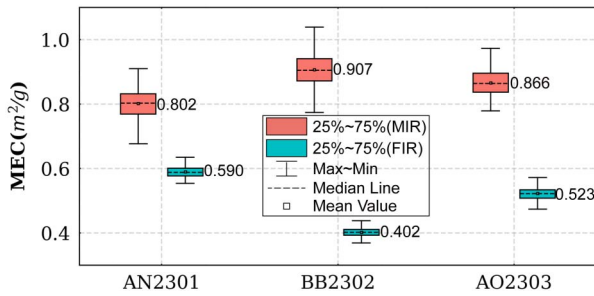
Fig. 7. Average MECs of aggregates in the MIR and FIR.

Fig. 9. Transmittances of three materials in the MIR and FIR.

group compositions and generally have similar absorption abilities, but exhibit different scattering abilities due to differences in particle size and spatial structure of aggregates. The closer the size of the aggregates is to half the wavelength of light, the stronger the scattering ability. Among the three materials, the particle size of BB2302 is the smallest, so the scattering ability is also weakest in the 8–14 µm waveband.

As shown in Fig. 7, based on the calculated results, the MECs of aggregates of the three materials generally conform to the law of normal distribution, their mean values in the MIR are $0.802\,\text{m}^2/\text{g}$, $0.907\,\text{m}^2/\text{g}$, and $0.866\,\text{m}^2/\text{g}$, respectively, and their mean values in the FIR are $0.590\,\text{m}^2/\text{g}$, $0.402\,\text{m}^2/\text{g}$, and $0.523\,\text{m}^2/\text{g}$, respectively. The extinction performance of the three materials in the MIR is better than that in the FIR.

3.2. Validation of results

A large smoke box experimental system $(4\,\text{m} \times 3\,\text{m} \times 2.4\,\text{m})$ is shown in Fig. 8. Infrared radiation sources and detectors were placed on both sides of the smoke box. The light path between the infrared radiation source and the corresponding detector was 3 m. Two high-precision blackbody radiation sources (Fuyuan blackbody HFX-300A) were used to provide infrared radiation with constant temperature. Two infrared thermal imagers, FLIR SC7700 and VarioCAM HD875, were used to detect the radiation intensity on the target radiation source in the MIR and FIR, respectively. An intelligent particle sampler (Model LB-120-F) was installed inside the smoke box to constitute the concentration sampling system. In the experiments, the material samples were sprayed through the nozzle
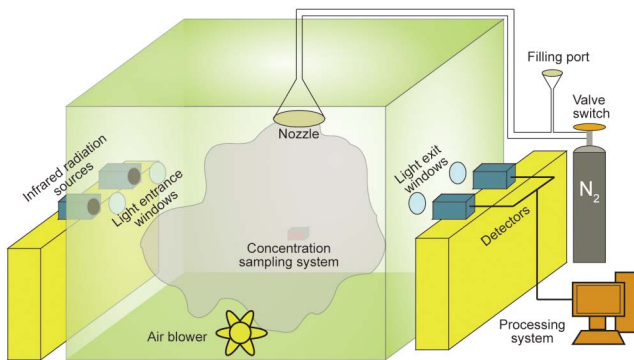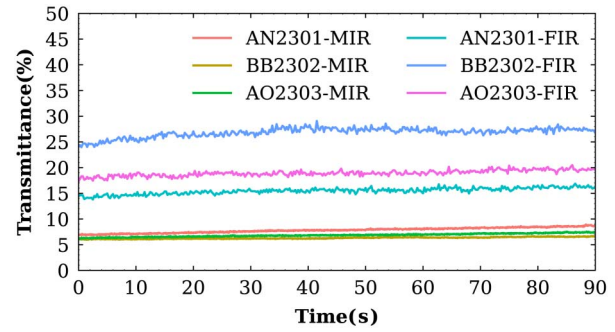
using nitrogen gas at 10 MPa. When the materials in the smoke box were evenly distributed, the concentration sampling system starts to operate at a flow rate of 100 L per minute, with a sampling time of 3 min. The weight of the filter membrane before and after sampling is measured by a high-precision electronic balance. Based on the weight difference of the filter membrane before and after sampling and the gas extraction volume, the mass concentration of the material can be calculated. The infrared thermal images on the target radiation source were recorded by detectors before and after the release of material. The transmittance of material in the MIR and FIR can be derived in terms of measurements of the radiation intensity on the target radiation source of the infrared thermal images.

Materials were weighed as 50 g with an electronic balance and filled in the filling port of the smoke box. Based on plentiful experimental results, it can be estimated that approximately 60%–70% of the initial mass of materials was stably dispersed in the smoke box. The mass concentrations of the three materials in the smoke box were $1.108\,\text{g}/\text{m}^3$, $1.105\,\text{g}/\text{m}^3$, and $1.126\,\text{g}/\text{m}^3$, respectively. The transmittances of the three materials in the smoke box experimental system are plotted in Fig. 9.

The average MEC of the material is an intrinsic physical parameter to represent the extinction property of material and can be obtained based on the Beer–Lambert law. According to the above experimental data, the average MECs of the three materials in the MIR and FIR are shown in Fig. 10.

Due to sedimentation and the dynamic changes of biological aggregation particles during the transmittance measurement,
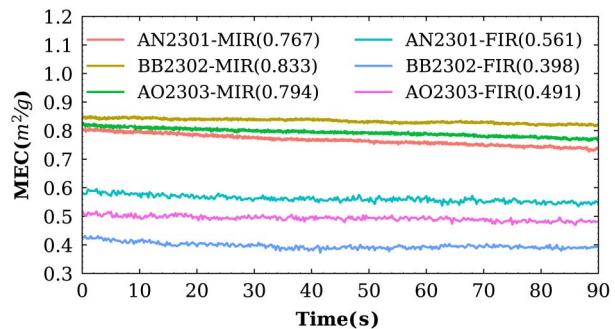

Fig. 8. Smoke box experimental system.

Fig. 10. Average MECs of three materials in the MIR and FIR. The mean values of the average MECs are shown in parentheses.

Table 2. Comparison of Calculated Average MECs (MEC_T) and Experimental Results (MEC_E).

Material	3–5 μm			8–14 μm		
	MEC_T (m^2/g)	MEC_E (m^2/g)	DEV	MEC_T (m^2/g)	MEC_E (m^2/g)	DEV
AN2301	0.802	0.767	4.56%	0.590	0.561	5.17%
BB2302	0.907	0.833	8.88%	0.402	0.398	1.01%
AO2303	0.866	0.794	9.07%	0.523	0.491	6.52%

with a certain deviation between the real-time concentration and the sampling concentration, the test results may inevitably have some errors. As shown in Table 2, the overall deviation is within 10%. The theoretical calculation results and test results based on smoke box experiments have good consistency.

Therefore, this method can be used to accurately predict the actual extinction performance of non-spherical biological particle materials. We can test the reflectance spectrum of various prepared non-spherical biological particle materials, calculate their complex refractive index, and observe their particle morphology through electron microscopy. By constructing a certain number of particle aggregates, we can estimate the extinction performance of materials, thereby quickly completing the screening of strong extinction materials.

4. Conclusion

In summary, comprehensively considering the morphology of particles, the complex refractive index of materials, and the randomly oriented aggregation of biological particles, a method to accurately calculate the extinction performance parameters of non-spherical biological particle materials was proposed. The theoretical calculation MECs and experimental results are shown in Table 2. The reasonable agreement between experimental data and theoretical results indicates the feasibility and effectiveness of the method, which provides a promising platform for further exploitation of the optical properties of various non-spherical biological particle materials.

Acknowledgement

References

1. Y. Hu, X. Zhao, Y. Gu, X. Chen, X. Wang, P. Wang, Z. Zheng, and X. Dong, "Significant broadband extinction abilities of bioaerosols," Sci. China Mater. **62**, 1033 (2019).
2. P. Wang, H. Liu, Y. Zhao, Y. Gu, W. Chen, L. Wang, L. Li, X. Zhao, W. Lei, Y. Hu, and Z. Zheng, "Electromagnetic attenuation characteristics of microbial materials in the infrared band," Appl. Spectrosc. **70**, 1456 (2016).
3. Y. Gu, W. Lu, J. Fang, C. Zheng, X. Chen, X. Wang, and Y. Hu, "Research progress on artificially prepared infrared extinction materials and their extinction properties (Invited)," Infrared Laser Eng. **49**, 20201018 (2020).
4. Y. Gu, Y. Hu, X. Zhao, X. Chen, P. Wang, and Z. Zheng, "Discrimination of viable and dead microbial materials with Fourier transform infrared spectroscopy in 3-5 micrometers," Opt. Express **26**, 15842 (2018).
5. X. Wang, Y. Hu, Y. Gu, X. Zhao, and X. Chen, "Effects of relative humidity on the broadband extinction performance of bioaerosol," Opt. Express **27**, 23801 (2019).
6. J. Fröhlich-Nowoisky, C. J. Kampf, B. Weber, J. A. Huffman, C. Pöhlker, M. O. Andreae, N. Lang-Yona, S. M. Burrows, S. S. Gunthe, W. Elbert, H. Su, P. Hoor, E. Thines, T. Hoffmann, V. R. Després, and U. Pöschl, "Bioaerosols in the Earth system: climate, health, and ecosystem interactions," Atmos. Res. **182**, 346 (2016).
7. X. Zhao, Y. Hu, Y. Gu, and L. Li, "Transmittance of laser in the microorganism aggregated particle swarm," Acta Opt. Sin. **35**, 0616001 (2015).
8. W. Ding, Y. Gu, Y. Hu, J. Fang, W. Lu, X. Wang, and X. Chen, "Optimized shape and structure of artificial bioparticles to enhance the optical extinction properties," Opt. Eng. **61**, 095109 (2022).
9. Y. Hu, B. Huang, Y. Gu, and Y. Zhao, "Model construction of biological particles' average extinction efficiency factor in far infrared band," Infrared Laser Eng. **47**, 1004003 (2018).
10. X. Zhao, Y. Hu, Y. Gu, X. Chen, X. Wang, P. Wang, and X. Dong, "Aggregation-driven reductions in the mass extinction coefficient of bioaerosols," Optik **184**, 115 (2019).
11. L. Li, Y. Hu, Y. Gu, X. Zhao, S. Xu, L. Yu, Z. M. Zheng, and P. Wang, "Infrared extinction performance of randomly oriented microbial-clustered agglomerate materials," Appl. Spectrosc. **71**, 2555 (2017).
12. W. Lu, Y. Gu, J. Fang, Y. Hu, W. Ding, X. Wang, and X. Chen, "10.6 μm laser extinction performance of polydisperse biological aggregate particles," Chin. J. Lasers **48**, 0401019 (2021).
13. W. Ding, Y. Gu, Y. Hu, G. Chen, H. Cao, and H. He, "Ballistic cluster–cluster aggregation model optimization," AIP Adv. **13**, 035017 (2023).
14. C. Li and H. Xiong, "3D simulation of the cluster–cluster aggregation model," Comput. Phys. Commun. **185**, 3424 (2014).
15. Y. Wu, T. Cheng, L. Zheng, and H. Chen, "Effect of morphology on the optical properties of soot aggregated with spheroidal monomers," J. Quant. Spectrosc. Radiat. Transf. **168**, 158 (2016).
16. J. Perry, J. Kimery, L. S. Matthews, and T. W. Hyde, "Effects of monomer shape on the formation of aggregates from a power law monomer distribution," New J. Phys. **15**, 073026 (2013).
17. H. Q. Ma, L. Y. Zhou, Z. H. Liu, M. Y. Chen, X. H. Xia, and Y. Z. Zhao, "A review of recent development for the CFD-DEM investigations of non-spherical particles," Powder Technol. **412**, 117972 (2022).
18. M. A. El-Emam, L. Zhou, W. Shi, C. Han, L. Bai, and R. Agarwal, "Theories and applications of CFD–DEM coupling approach for granular flow: a review," Arch. Comput. Methods Eng. **28**, 4979 (2021).
19. B. T. Draine, "The discrete-dipole approximation and its application to interstellar graphite grains," Astrophys. J. **333**, 848 (1988).
20. H. Liu, P. Wang, Y. Hu, G. Zhao, H. Liu, Z. Li, H. Wu, L. Wang, and Z. Zheng, "Optimised fermentation conditions and improved collection efficiency using dual cyclone equipment to enhance fungal conidia production," Biocontrol Sci. Technol. **25**, 1011 (2015).
21. M. Lattuada, H. Wu, and M. Morbidelli, "Radial density distribution of fractal clusters," Chem. Eng. Sci. **59**, 4401 (2004).
22. T. Kozasa, J. Blum, and T. Mukai, "Optical properties of dust aggregates. I. Wavelength dependence," Astron. Astrophys. **263**, 423 (1992).
23. T. Kozasa, J. Blum, H. Okamoto, and T. Mukai, "Optical properties of dust aggregates. II. Angular dependence of scattered light," Astron. Astrophys. **276**, 278 (1993).
24. C. Huang, Z. Wu, Y. Liu, and S. Long, "Effect of porosity on optical properties of aerosol aggregate particles," Acta Opt. Sin. **33**, 0129001 (2013).
25. P. Grosse and V. Offermann, "Analysis of reflectance data using the Kramers–Kronig relations," Appl. Phys. A **52**, 138 (1991).

26. H. C. Booij and G. P. J. M. Thoone, "Generalization of Kramers–Kronig transforms and some approximations of relations between viscoelastic quantities," Rheol. Acta **21**, 15 (1982).

27. O. Meitav, O. Shaul, and D. Abookasis, "Determination of the complex refractive index segments of turbid sample with multispectral spatially modulated structured light and models approximation," J. Biomed Opt. **22**, 097004 (2017).

28. M. Segal-Rosenheimer and R. Linker, "Impact of the non-measured infrared spectral range of the imaginary refractive index on the derivation of the real refractive index using the Kramers–Kronig transform," J. Quant. Spectrosc. Radiat. Transf. **110**, 1147 (2009).

29. Y. Gu, Y. Hu, X. Zhao, and X. Chen, "Determination of infrared complex refractive index of microbial materials," J. Quant. Spectrosc. Radiat. Transf. **217**, 305 (2018).

30. M. J. Collinge and B. T. Draine, "Discrete-dipole approximation with polarizabilities that account for both finite wavelength and target geometry," J. Opt. Soc. Am. A **21**, 2023 (2004).

31. B. T. Draine and P. J. Flatau, "Discrete-dipole approximation for periodic targets: theory and tests," J. Opt. Soc. Am. A **25**, 2693 (2008).

32. B. T. Draine and P. J. Flatau, "Discrete-dipole approximation for scattering calculations," J. Opt. Soc. Am. A **11**, 1491 (1994).